

Prediction of Grain Growth Behavior in HAZ During Gas Tungsten Arc Welding of 304 Stainless Steel

H. Jamshidi Aval, S. Serajzadeh, and A.H. Kokabi

(Submitted June 8, 2008; in revised form January 16, 2009)

In this study, the thermal cycles and the grain structure in the weld heat-affected zone (HAZ) are predicted. At the first stage, a combined heat transfer and fluid flow model is employed to assess the temperature fields during and after welding of 304 stainless steel and then, the evolution of grain structure is conducted using the predicted temperature distribution and an analytical model of grain growth. The grain sizes of the CGHAZ (coarse grain heat affected zone) achieved from the model are basically in agreement with those obtained from experimental measurement under different heat inputs in the range of 0.33–1.07 MJ/m. Both the experimental data and the calculated results show that the average grain size near the fusion plane is about two to four times larger than the average grain size in the base plate depending on the applied heat input.

Keywords gas tungsten arc welding, grain growth, mathematical modelling, 304 stainless steel alloy

1. Introduction

It is established that welding heat input significantly affects the microstructure and mechanical properties of the heat-affected zone (HAZ). Especially, the heat input increases the kinetics of grain growth in the region near the fusion line, called the coarse grain heat affected zone (CGHAZ). On the other hand, grain structure affects the strength, toughness, ductility, and corrosion resistance of alloys (Ref 1). This is because the modeling of microstructural changes within the welded materials is of importance to engineers and scientists. In recent years, significant contributions have been made to understand thermal and metallurgical behavior of metals and alloys during welding processes using numerical techniques. Different models and techniques have been employed to simulate arc welding processes and various types of physical phenomena have been predicted. For instance, Chakraborty and Chakraborty (Ref 2) have investigated the effects of positive and negative surface tension coefficients on both laminar and turbulent weld pool convection for a typical gas tungsten arc welding (GTAW) process. Chakraborty et al. (Ref 3) have presented a modified k - ϵ model capable of considering turbulent weld-pool convection in the presence of a continuously evolving phase-change interface in GTAW process. Kubiszyn and Slania (Ref 4) have proposed a model to predict physical phenomena during welding operations of steels including temperature variations and diffusion. Taylor et al. (Ref 5) have presented a numerical model to determine fluid flow, temperature field, and residual stresses in welding processes

using the finite volume method. Chakraborty and Chakraborty (Ref 6) have determined the effects of turbulence on momentum, heat, and mass transfer during laser welding of a copper-nickel dissimilar couple. Many other studies have also been conducted to predict macro-parameters such as temperature and velocity fields during welding processes (Ref 7–12). In addition, metallurgical events and phase transformations during and after welding processes have been investigated. Ashby and Easterling (Ref 13) and Ion et al. (Ref 14) have established a mathematical model for computing the microstructure and hardness of the HAZ for micro-alloyed steels based on phase transformation dynamics. Recently, the Monte Carlo techniques have also been applied to determine grain growth kinetics in the HAZ of a weldment in two and three dimensions (Ref 15–18). Pathak and Datta (Ref 19) have determined microstructures developed after submerged arc welding employing three-dimensional finite element analysis. Watt et al. (Ref 20) have developed an algorithm to predict microstructural development in the HAZ in welding processes of low alloy steels. Choi and Mazumder (Ref 21) have analyzed solidification behavior and residual stresses in GMAW process of 304 stainless steel. Farzadi et al. (Ref 22) have predicted solidification behavior of an aluminum alloy by coupling phase field and CFD techniques.

In this study, an attempt has been made to estimate the grain growth distribution in the HAZ in GTAW of 304 stainless steel. Grain size in the HAZ have been experimentally determined for the 304 stainless steel alloy weldment manufactured by GTAW at various heat inputs. Then, a three-dimensional heat transfer and fluid flow model is performed to calculate the temperature field and thermal cycles. The calculated thermal cycles are then used in an analytical model to simulate grain structure in the HAZ. At the final step, the model predictions of grain size are compared with the corresponding experimental results.

2. Mathematical Model

The temperature distribution and the determination of weld pool geometry may be calculated by the three-dimensional heat

H. Jamshidi Aval, S. Serajzadeh, and A.H. Kokabi, Department of Materials Science and Engineering, Sharif University of Technology, Azadi Ave., P.O. Box 11365-9466, Tehran, Iran. Contact e-mail: serajzadeh@sharif.edu.

transfer and fluid flow model assuming a Newtonian liquid flow in the weld pool. In this regard, the flow of liquid metal in the weld pool may be described by the following equation:

$$\rho(\vec{V} \cdot \nabla)\vec{V} = \vec{F}_b - \nabla P + \mu \nabla^2 \vec{V} \quad (\text{Eq 1})$$

Body force is determined by the following equations:

$$\begin{aligned} \vec{F}_b &= \vec{F}_{\text{emf}} - F_b \\ \vec{F}_{\text{emf}} &= \vec{J} \times \vec{B} \\ F_b &= \rho \cdot g \cdot \beta \cdot \Delta T \end{aligned} \quad (\text{Eq 2})$$

where ρ is the density, \vec{V} is the velocity vector, F_b is the Buoyancy Force, P is the pressure, μ is the viscosity, F_{emf} is the electromagnetic force, J is the current density, B is the magnetic field, g is the gravitational acceleration, β is the thermal expansion exponent, and T is the temperature. The following equations are then solved to obtain the magnetic field:

$$\nabla \times \vec{B} = \mu_m \vec{J} \quad (\text{Eq 3})$$

$$\nabla \cdot \vec{J} = 0 \quad (\text{Eq 4})$$

where μ_m is the magnetic permeability while the mass conservation can be represented by the following equation:

$$\nabla \cdot \vec{V} = 0 \quad (\text{Eq 5})$$

It should be noted that the electromagnetic force was first determined by solving Maxwell's equation, and then the fields of "J" and "B" in Eq 3 and 4 have been calculated by a user-defined function employing the calculated electromagnetic force.

In order to trace the weld pool liquid/solid interface, the total enthalpy H is calculated by the sum of the sensible heat, h , and the latent heat content, ΔH , i.e., $H = h + \Delta H$. The sensible heat h is expressed as $h = \int C_p dT$, where C_p is the specific heat, and T is the temperature. The latent heat content, ΔH , is calculated as $\Delta H = f_L \cdot L$, where L is the latent heat of fusion. The liquid fraction, f_L , is assumed to be varying linearly versus temperature as follows (Ref 23):

$$f_L = \begin{cases} 1, & T > T_L \\ \frac{T - T_S}{T_L - T_S}, & T_S \leq T \leq T_L \\ 0, & T < T_S \end{cases} \quad (\text{Eq 6})$$

where T_L and T_S are the liquidus and the solidus temperatures, respectively. The thermal energy transportation in the weld work-piece is expressed by the following modified energy equation:

$$\rho \cdot C_p (\vec{V} \cdot \nabla T) = \nabla \cdot (k \nabla T) + Q_h \quad (\text{Eq 7})$$

where k is the thermal conductivity. The source term Q_h is given as follow (Ref 24):

$$Q_h = -\rho \frac{\partial \Delta H}{\partial t} - \rho \nabla \cdot (V \Delta H) \quad (\text{Eq 8})$$

Note that the source term, Q_h , is given as Eq 8 is in a general form and consists of both transient and steady state terms; however, only the steady-state part has been applied in the model under this study.

A three-dimensional Cartesian coordinate system is employed in the calculation, while only half of the work-piece is considered since the weld is symmetrical about the weld

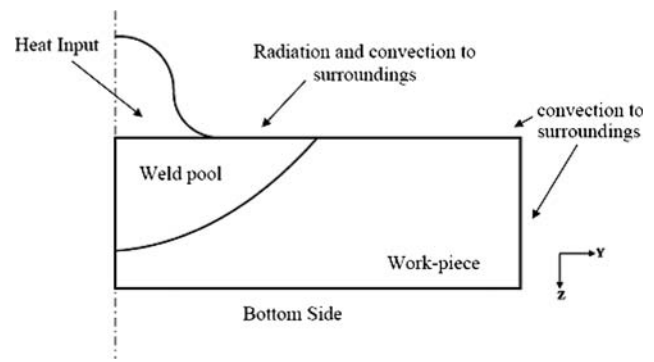


Fig. 1 A schematic plot of the weld cross section showing boundary conditions used in the calculation

Table 1 Physical properties of 304 stainless steel

Property/parameter	Value
Density of liquid, kg/m ³	7.2 × 10 ³
Effective viscosity, kg/m s	0.1
Solidus temperature, K	1697
Liquidus temperature, K	1727
Temperature coefficient of surface tension, N/m K	-0.43 × 10 ⁻³
Coefficient of thermal expansion	1.96 × 10 ⁻⁵

Table 2 Kinetic parameters for grain growth

T, °C	n	k
1000	6.4	3.20E-15
1200	5	4.40E-15
1400	4.5	5.20E-15
1424	4	5.40E-15

center line. Figure 1 is a schematic illustration showing the governing boundary conditions. These boundary conditions are further discussed as follows.

The weld top surface is assumed to be flat. The velocity boundary condition is given as:

$$\mu \frac{\partial u}{\partial z} = \frac{\partial \gamma}{\partial T} \cdot \frac{\partial T}{\partial x} \cdot f_L \quad (\text{Eq 9})$$

$$\mu \frac{\partial v}{\partial z} = \frac{\partial \gamma}{\partial T} \cdot \frac{\partial T}{\partial y} \cdot f_L \quad (\text{Eq 10})$$

$$w = 0 \quad (\text{Eq 11})$$

where u , v , and w are the velocity components along the x , y , and z directions, respectively, and $d\gamma/dT$ is the temperature gradient of surface tension coefficient (Ref 24). The heat flux at the top surface is given as:

$$K \frac{\partial T}{\partial z} = q(r) - \sigma \varepsilon (T^4 - T_0^4) - h_c (T - T_0) \quad (\text{Eq 12})$$

$$q(r) = \frac{\eta \cdot U_w I}{2\pi \cdot r_b^2} \exp\left(-\frac{r^2}{2 \cdot r_b^2}\right) \quad (\text{Eq 13})$$

where q is heat flux (Ref 25), η is the arc efficiency, U_w is the welding speed, I is the welding current, r_b is the heat distribution parameter, r is the distance between the specific

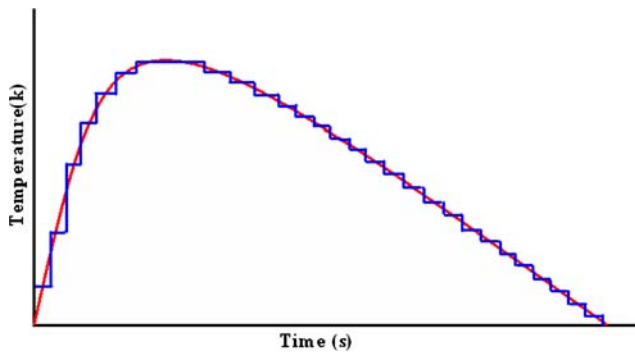


Fig. 2 Discretization of the continuous thermal cycle

Table 3 Welding parameters

Weld No.	Heat input, MJ/m	Current, A	Voltage, V	Speed, cm/min
1	0.49	110	11.5	10
2	0.328	110	11.5	15
3	0.726	150	12.6	10
4	0.487	150	12.6	15
5	1.069	200	13.8	10
6	0.717	200	13.8	15

Table 4 The arc efficiency at various conditions

η	Current, A	Speed, cm/min
0.82	110	10
0.85	110	15
0.77	150	10
0.8	150	15
0.71	200	10
0.74	200	15

location and the heat source, σ is the Stefan-Boltzmann constant, h_c is the convective heat transfer coefficient, and T_0 is the ambient temperature. At the $y = 0$ and symmetric surface:

$$\frac{\partial T}{\partial y} = 0 \quad (\text{Eq 14})$$

$$\frac{\partial u}{\partial y} = 0, \quad v = 0, \quad \frac{\partial w}{\partial y} = 0 \quad (\text{Eq 15})$$

On the other surfaces except for $z = 0$, the following boundary condition has been utilized:

$$K\nabla T = -\alpha(T - T_0) \quad (\text{Eq 16})$$

where α is the effective heat transfer coefficient describing the effects of conduction and radiation. Note that the above heat transfer and the fluid flow equations have been solved by the finite volume code Fluent. The dimensions of the physical domain were 400 mm (length) \times 100 mm (width) \times 6 mm (thickness). The number of grids was 331056. Spatially non-uniform grids were used owing to non-uniform distributions of velocities and temperature where finer grids were used near the heat source region. The physical properties of the steel are given in Table 1 while utilized heat conduction coefficient and specific heat are as follows:

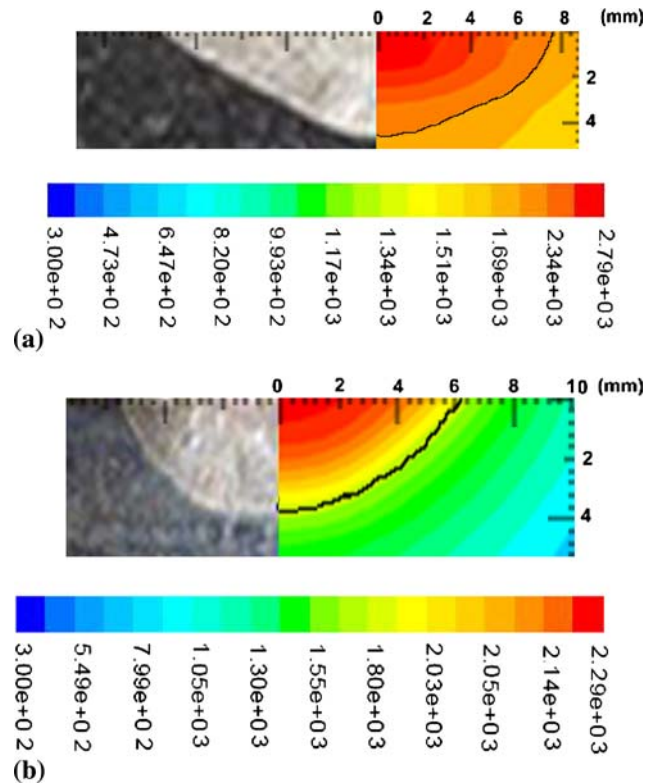


Fig. 3 Computed and experiment weld pool geometry under different welding speeds, (a) $I = 200$ A, $V = 10$ cm/min, Heat Input = 1.069 MJ/m, (b) $I = 200$ A, $V = 15$ cm/min, Heat Input = 0.717 MJ/m

$$\begin{aligned} T < 373^\circ\text{K} & \quad k = 15 \text{ W/m}^\circ\text{K} \\ 373 \leq T < 573 & \quad k = 0.01 T + 11.27 \text{ W/m}^\circ\text{K} \\ 573 \leq T < 1697 & \quad k = 0.002 T + 15.85 \text{ W/m}^\circ\text{K} \\ 1697 \leq T < 1727 & \quad k = 6.33 T - 10731 \text{ W/m}^\circ\text{K} \\ T \geq 1727^\circ\text{K} & \quad k = 209.3 \text{ W/m}^\circ\text{K} \end{aligned} \quad (\text{Eq 17})$$

$$\begin{aligned} T < 373 \text{ K}, & \quad c_p = 500 \text{ J/kg K} \\ 373 < T < 1697, & \quad c_p = 0.1612T + 438.27 \text{ J/kg K} \\ 1697 < T < 1727, & \quad c_p = 4.19T - 6393 \text{ J/kg K} \\ T > 1727, & \quad c_p = 837.4 \text{ J/kg K} \end{aligned} \quad (\text{Eq 18})$$

Utilizing the predicted temperature field, the fusion zone geometry was determined by the solidus temperature, i.e., 1697 K.

After obtaining the steady-state temperature field, the thermal cycle at a given location such as (x, y, z) may be calculated using the following equation:

$$T(x, y, z, t_2) = \frac{T_s(\zeta_2, y, z) - T_s(\zeta_1, y, z)}{\zeta_2 - \zeta_1} V_s(t_2 - t_1) + T(x, y, z, t_1) \quad (\text{Eq 19})$$

where $T(x, y, z, t_1)$ and $T(x, y, z, t_2)$ are the temperatures at time t_1 and t_2 , respectively, $T_s(\zeta_1, y, z)$ and $T_s(\zeta_2, y, z)$ are the steady-state temperatures at coordinates (ζ_1, y, z) and (ζ_2, y, z) , respectively, V_s is the welding speed, and $(\zeta_2 - \zeta_1)$ is the length welded in time $(t_1 - t_2)$ (Ref 9).

An important phenomenon during and after welding processes is the grain growth in the HAZ, which where subjected to large temperature variations. In the HAZ, this phenomenon occurred under non-isothermal conditions, and depending on

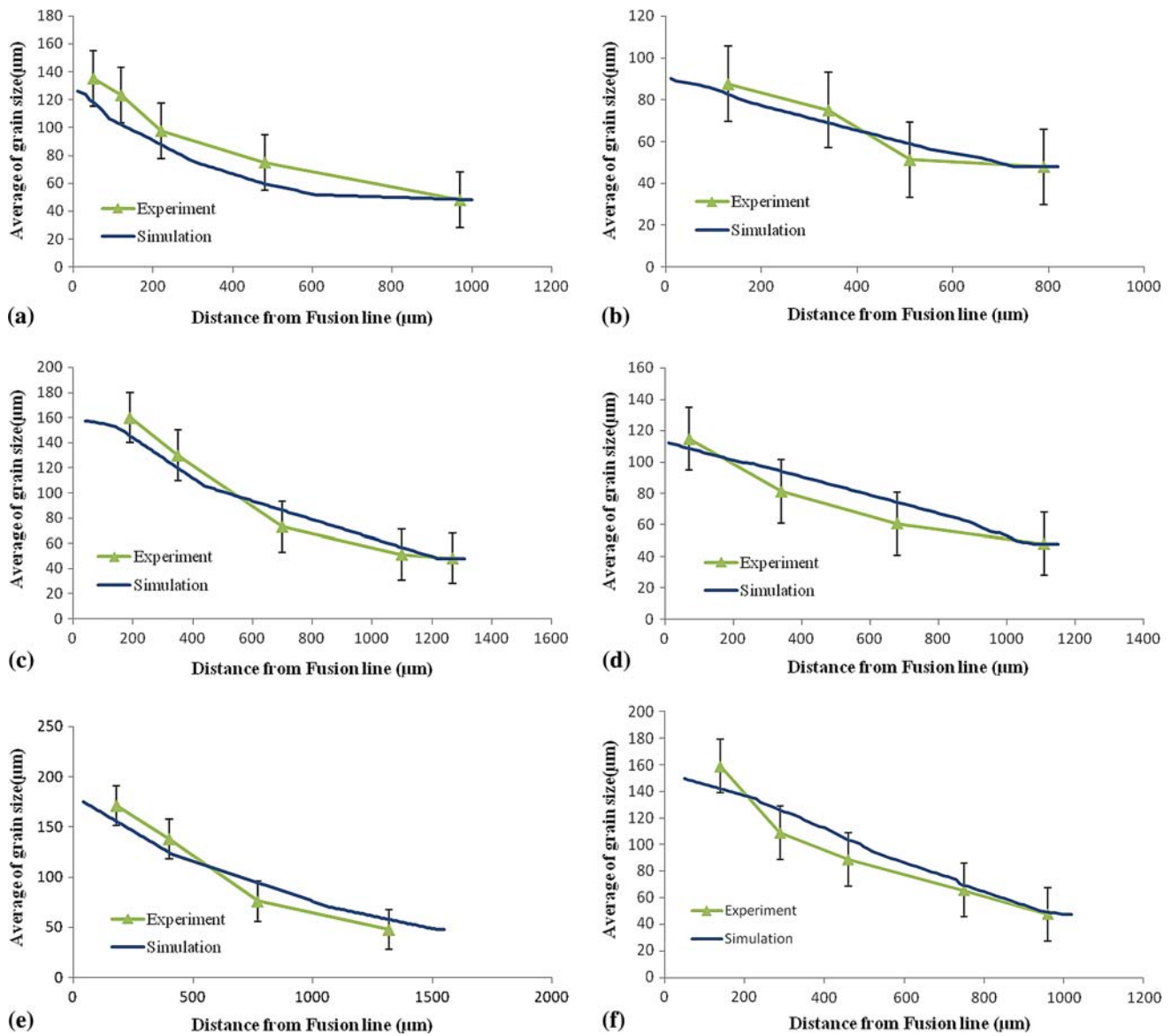


Fig. 4 Computed and experimental grain sizes in the HAZ weld based on the parameters mentioned in Table 3, (a) Sample 1, (b) Sample 2, (c) Sample 3, (d) Sample 4, (e) Sample 5, and (f) Sample 6

Table 5 Comparison of the size of weld pool with the experimental observation

Difference, %	Penetration, mm		Difference, %	Width, mm		Heat input, MJ/m	Weld No.
	Simulation	Experiment		Simulation	Experiment		
22.2	2.8	3.6	7.4	5	5.4	0.49	1
9.1	2	2.2	4.5	4.2	4.4	0.328	2
21.7	3.6	4.6	11.1	6.4	7.2	0.726	3
21.9	3.2	4.1	1.7	5.7	5.8	0.487	4
8.3	4.4	4.8	21.8	7.5	9.6	1.069	5
25	3.5	4.4	8.7	6.3	5.7	0.717	6

the employed welding parameters and materials properties, notable variations in grain structure can be observed. Therefore, to predict the grain growth behavior in HAZ, it is vital to know the temperature history as well as the kinetics of grain growth.

The thermal cycles and temperature histories in different points of welded metal can be obtained by the above-mentioned model. On the other hand the kinetics of grain growth should be determined by experiments. In order to achieve the kinetics of

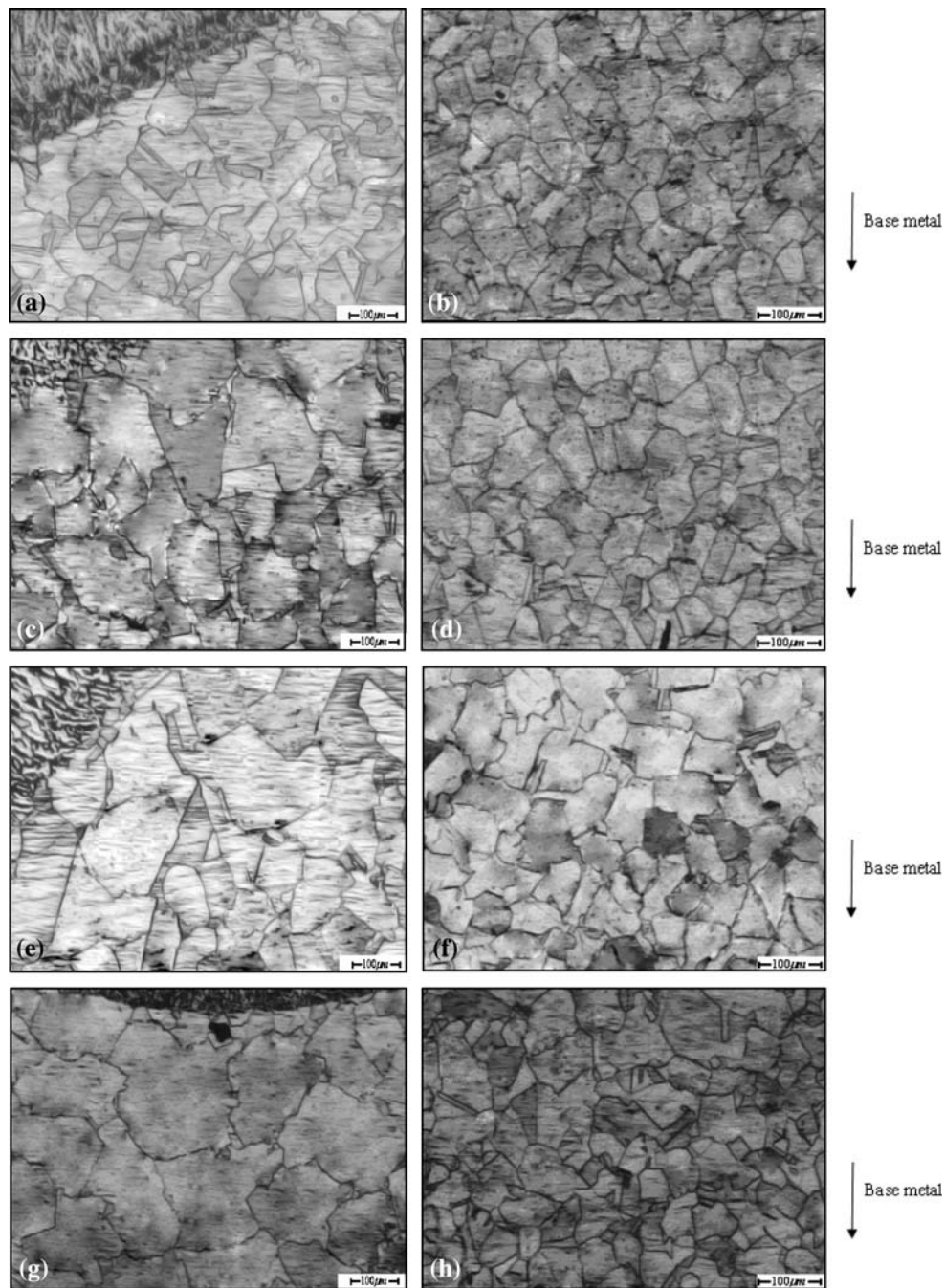


Fig. 5 Typical austenite grains in CGHAZ for different heat inputs (a) Sample 2, (c) Sample 4, (e) Sample 5, and (g) Sample 6, and typical austenite grains in HAZ near to base metal under different heat inputs (b) Sample 2, (d) Sample 4, (f) Sample 5, and (h) Sample 6

grain growth during welding process, the experimental measurements of grain size at given temperatures and different holding times were carried out, and it was found that there exists a relation between the current grain size, \bar{R}_{i+1} , initial grain size, \bar{R}_i , holding time, t , and temperature, T , as follows:

$$\bar{R}_{i+1}^{n(T_{i+1})} - \bar{R}_i^{n(T_{i+1})} = k(T_{i+1})t \quad (\text{Eq 20})$$

Here k and n are dependent on temperature. Both k and n are obtained from experimental data while their values are given in Table 2.

Although the high spatial temperature gradient exists in the weldment, with discretization of the continuous heating and cooling curves, as shown in Fig. 2, Eq 20 can be used in prediction of grain size in the HAZ. The time step was small enough to account for the severe temperature variations during a single thermal cycle. After the fluid flow and heat transfer equations were solved under steady-state conditions using Fluent, the temperature distribution was converted into time-dependent data employing Eq 19 and then imported into Matlab where Eq 20 was utilized to find mean grain size variations as a function of temperature.

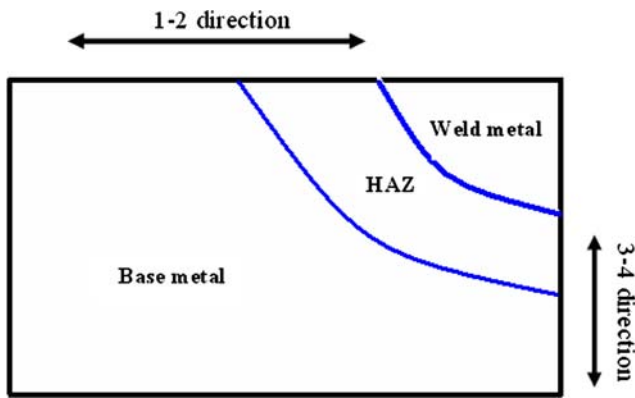


Fig. 6 Directions used in calculation of grain size

3. Experimental Procedure

Gas tungsten arc welds have been performed on plate samples of 304 stainless steel alloy. The composition of alloy is (in wt.%): 1.05% Mn, 18.3% Cr, 8.84% Ni, 0.0262% P, 0.0043% S, and balance Fe. The steel plate thickness was 6 mm where no preheating was employed in the experiments. High purity Argon was used as the welding gas, and the welding parameters used in the experiments are listed in Table 3. The arc efficiency at various welding conditions are listed in Table 4. Optical metallography was also performed on pre- and post-weld samples using conventional polishing and etching techniques. Different etchants were utilized to reveal the weld pool boundary and the grain boundary structures. The best results for etching of the weld pool boundary and grain boundaries were obtained by applying 15 mL HCl, 5 mL HNO₃, and 100 mL H₂O. In addition, the average grain size at various distances from the fusion line was measured using the intercept method (Ref 26). In order to determine the kinetics of austenite grain growth, additional experiments were also performed. The samples at different temperatures and times were heated in the furnace and then air cooled to room temperature and then the average grain sizes of the samples were measured using the intercept method.

4. Modelling Results

The calculated bead shape and temperature fields are presented in Fig. 3. The weld pool boundary is represented by the solidus temperature isotherm at 1697 K. The experimental result was obtained by measuring the fusion boundary by means of metallographical studies. It can be seen that these two sets of results are in good agreement. Besides, Table 5 compares the predicted and the measured sizes of the weld pools under different welding conditions, which also show a reasonable agreement.

Both the experimental data and the predicted results show the important geometrical factors of the weld bead. For instance, penetration depth of the weld pool increases with the applied electrical current. When the current is increased, the liquid metal falls along the pool axis and rises along the pool boundary. The electrical current converges from the work-piece

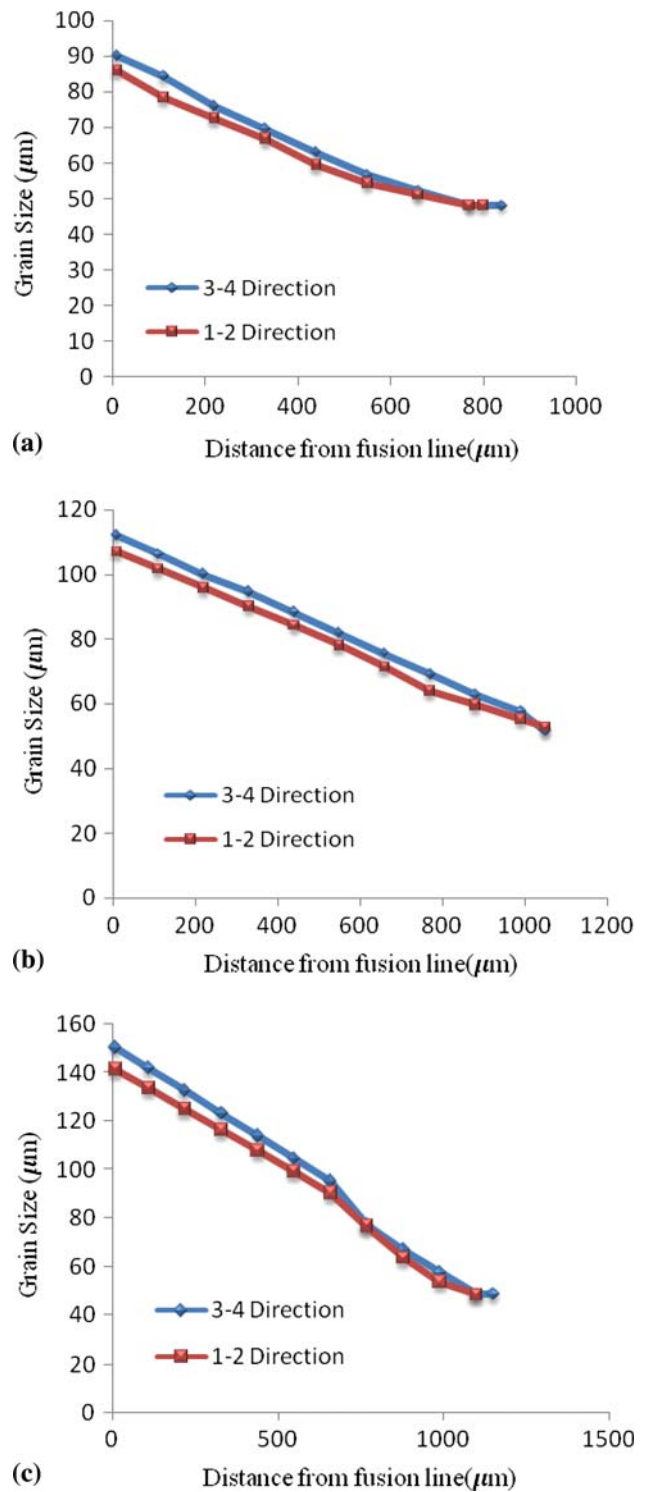


Fig. 7 Predicted spatial distribution of grain size in the HAZ weld using the parameters mentioned in Table 3, (a) Sample 2, (b) Sample 4, and (c) Sample 6

to the center of the pool surface. Thus, it pushes the liquid downward along the pool axis and makes the weld pool deeper owing to the resulting Lorentz force. Furthermore, the computed results and the experimental data show a reduction in penetration depth with an increase in the welding speed. However, the depth of penetration is not significantly affected

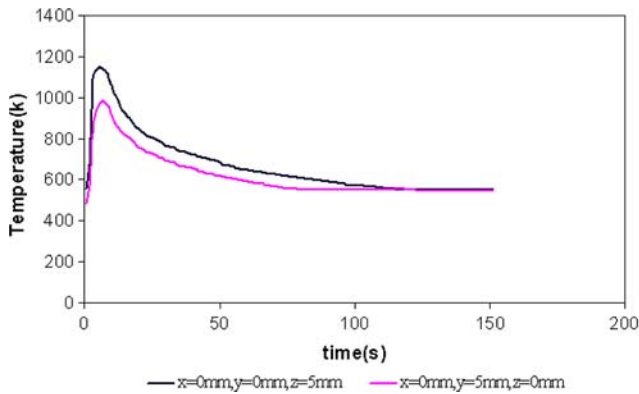


Fig. 8 Computed thermal cycles in two points in sample 6

by the welding speed. The most significant effect of welding speed is its influence on the volume of the weld pool. With increase in the welding speed, amount of heat input is decreased and therefore the weld pool volume is reduced as shown in Fig. 3(a) for welding speed of 10 cm/min, and Fig. 3(b) for welding speed of 15 cm/min.

Figure 4 compares the grain size in the HAZ predicted by the model and the experimental data. Figure 5 also shows typical grain size structure at the regions near the fusion line. As expected, the grain size is changed significantly depending on the temperature and heat input. The results show that the higher heating temperature, the larger the final grain sizes. It is clear that the grain size is larger at the site near the fusion line than those located far from the fusion line. Furthermore, the width of the HAZ is increased with increasing the weld heat input.

Grain size variations have been predicted along at different regions. Figure 6 shows two different routes used in the modeling in order to study the effect of local variation in thermal cycles. The variations of the mean grain size versus distance from the fusion plane for the top surface, i.e., route: 1-2 and the mid-section vertical symmetry plane, route: 3-4, are shown in Fig. 7. It is found that the mean grain size at the same distance from the fusion line is different. For instance, along the route 1-2 the grain sizes are smaller than those along the route 3-4 in all the cases. Figure 8 shows thermal cycles in the above two points, and it can be observed that the thermal cycles in these points are different. As noted before, this behavior clearly indicates the strong influence of thermal cycle on the kinetics of grain growth in the HAZ.

5. Conclusions

A three-dimensional heat transfer and fluid flow model has been employed to determine the temperature history during and after tungsten arc welding of 304 Stainless Steel, and then the grain growth kinetics in the HAZ has been predicted employing the predicted thermal cycles and an analytical equation. The results show that

1. The calculated grain sizes at different heat inputs are comparable with the corresponding experimental results.
2. The average grain size near the fusion plane is about two to four times larger than that in the base plate depending

on the heat input used. The extent of grain growth in the HAZ is also strongly dependent on the heat input.

3. The mean grain size in regions equidistant from the fusion plane is increased along the circumferential direction from the top surface to the weld root. The higher temperature in the interior of the weldment than that at the top surface is responsible of this behavior.

References

1. J. Gao and R.G. Thompson, Real Time-Temperature Models for Monte Carlo Simulations of Normal Grain Growth, *Acta Metall.*, 1996, **44**, p 4565
2. N. Chakraborty and S. Chakraborty, Influences of Sign of Surface Tension Coefficient on Turbulent Weld Pool Convection in a Gas Tungsten Arc Welding (GTAW) Process, *Trans. ASME J. Heat Transfer*, 2005, **127**, p 848–862
3. N. Chakraborty, S. Chakraborty, and P. Dutta, Modelling of Turbulent Transport in Arc Welding Pools, *Int. J. Numer. Method Heat Fluid Flow*, 2003, **13**, p 7–30
4. I. Kubiszyn and J. Slania, Modelling Physical Phenomena of Welding Processes, *Weld. Int.*, 2003, **17**, p 89–93
5. G.A. Taylor, M. Hughes, N. Strusevich, and K. Pericleous, Finite Volume Methods Applied to the Computational Modelling of Welding Phenomena, *Appl. Math. Model.*, 2002, **26**, p 309–320
6. N. Chakraborty and S. Chakraborty, Modelling of Turbulent Molten Pool Convection in Laser Welding of a Copper-Nickel Dissimilar Couple, *Int. J. Heat Mass Transfer*, 2007, **50**, p 1805–1822
7. J. Goldak, A. Chakravarti, and M. Bibby, A new finite element model for welding heat sources, *Metall. Trans. B*, 1984, **15**, p 299
8. G.M. Oreper and J. Szekely, A Comprehensive Representation of Transient Weldpool Development in Spot Welding Operations, *Metall. Trans. A*, 1987, **18A**, p 1325–1332
9. K. Mundra, T. DebRoy, and K.M. Kelkar, Numerical Prediction of Fluid Flow and Heat Transfer in Welding with a Moving Heat Source, *Numer. Heat Transfer A*, 1996, **29**, p 115–129
10. I.S. Kim and A. Basu, A Mathematical Model of Heat Transfer and Fluid Flow in the Gas Arc Welding Process, *J. Mater. Process. Technol.*, 1998, **77**, p 17–24
11. N. Chakraborty and S. Chakraborty, Thermal Transport Regimes and Generalized Regime Diagrams for High Energy Surface Melting Processes, *Metall. Mater. Trans. B*, 2007, **38**, p 143–147
12. A. Farzadi, S. Serajzadeh, and A.H. Kokabi, Modeling of Heat Transfer and Fluid Flow During Gas Tungsten Arc Welding of Commercial Pure Aluminum, *Int. J. Adv. Manuf. Technol.*, 2008, **38**, p 258–267
13. M.F. Ashby and K.E. Easterling, A First Report on Diagram for Grain Growth in Welds, *Acta Metall.*, 1982, **30**, p 1969–1999
14. J.C. Ion, K.E. Easterling, and M.F. Ashby, A Second Report of Microstructure and Hardness Heat-affected Zones, *Acta Metall.*, 1984, **32**, p 1949–1962
15. S. Mishra and T. DebRoy, Measurements and Monte Carlo Simulation of Grain Growth in the Heat-affected Zone of Ti-6Al-4 V Welds, *Acta Mater.*, 2004, **52**, p 1183–1192
16. J. Gao, R.G. Thompson, and Y. Cao, Development of Monte Carlo Simulation of Grain Growth in HAZ, in *Trends in Welding Research*, H.B. Smartt, J.A. Johnson and S.A. David, Eds., ASM International, Materials Park, OH, 1996, p 199
17. B. Radhakrishnan and T. Zacharia, Simulation of Curvature-driven Grain Growth by Using a Modified Monte Carlo Algorithm, *Metall. Mater. Trans. A*, 1995, **26A**, p 167
18. A.L. Wilson, R.P. Martukanitz, and P.R. Howell, Experimental and Computer Simulation of Grain Growth in HSLA-100/80 Steels During Welding and Cladding, in *Trends in Welding Research*, J.M. Vitek, S.A. David, J.A. Johnson, H.B. Smartt, and T. DebRoy, Eds., ASM International, Materials Park, OH, 1998, p 161
19. A.K. Pathak and G.L. Datta, Three-dimensional Finite Element Analysis to Predict the Different Zones of Microstructure in Submerged Arc Welding, *Proc. Instn. Mech. Eng.*, 2004, **218**, p 269–280

20. D.F. Watt, L. Coon, M. Bibby, J. Goldak, and C. Henwood, An Algorithm for Modeling Microstructural Development in Weld Heat-affected Zones (Part A) Reaction Kinetics, *Acta Metall.*, 1988, **36**, p 3029–3035
21. J. Choi and J. Mazumder, Numerical and Experimental Analysis for Solidification and Residual Stress in the GMAW Process for AISI 304 Stainless Steel, *J. Mater. Sci.*, 2002, **37**, p 2143–2158
22. A. Farzadi, M. Do-Quang, S. Serajzadeh, A.H. Kokabi, and G. Amberg, Phase-field Simulation of Weld Solidification Microstructure in an Al-Cu Alloy, *Model. Simul. Mater. Sci. Eng.*, in press (doi: [10.1088/0965-0393/16/6/065005](https://doi.org/10.1088/0965-0393/16/6/065005))
23. W. Zhang, G.G. Roy, J.W. Elmer, and T. DebRoy, Modeling of Heat Transfer and Fluid Flow During Gas Tungsten Arc Spot Welding of Low Carbon Steel, *J. Appl. Phys.*, 2003, **93**, p 3022
24. R. Komanduri and Z.B. Hou, Thermal Analysis of the Arc Welding Process: Part I. General Solutions, *Metall. Mater. Trans. B*, 2000, **21B**, p 1353–1370
25. J. Jiadi and R. Dutta, Three-dimensional Turbulent Weld Pool Convection in Gas Metal Arc Welding Process, *Sci. Technol. Weld. Joining*, 2004, **9**, p 407–414
26. *Annual Book of ASTM Standards*, 1996, Vol. 1, Sect. 3, ASTM, West Conshohoken, PA